Atmos. Chem. Phys. Discuss., 15, 14505–14547, 2015
www.atmos-chem-phys-discuss.net/15/14505/2015/
doi:10.5194/acpd-15-14505-2015
© Author(s) 2015. CC Attribution 3.0 License.

Atmospheric Chemistry and Physics Discussions

This discussion paper is/has been under review for the journal Atmospheric Chemistry and Physics (ACP). Please refer to the corresponding final paper in ACP if available.

# Decadal trends in global CO emissions as seen by MOPITT

**Y. Yin[1], F. Chevallier[1], P. Ciais[1], G. Broquet[1], A. Fortems-Cheiney[2], I. Pison[1], and M. Saunois[1]**

[1]Laboratoire des Sciences du Climat et de l'Environnement, CEA-CNRS-UVSQ, UMR8212, Gif-sur-Yvette, France
[2]Institut National de l'Environnement Industriel et des RisqueS (INERIS), Verneuil-en-Halatte, France

Received: 20 April 2015 – Accepted: 4 May 2015 – Published: 22 May 2015

Correspondence to: Y. Yin (yi.yin@lsce.ipsl.fr)

Published by Copernicus Publications on behalf of the European Geosciences Union.







## Abstract

Negative trends of carbon monoxide (CO) concentrations are observed in the recent decade by both surface measurements and satellite retrievals over many regions, but they are not well explained by current emission inventories. Here, we attribute the observed CO concentration decline with an atmospheric inversion that simultaneously optimizes the two main CO sources (surface emissions and atmospheric hydrocarbon oxidations) and the main CO sink (atmospheric hydroxyl radical OH oxidation) by assimilating observations of CO and other chemically related tracers. Satellite CO column retrievals from Measurements of Pollution in the Troposphere (MOPITT), version 6, and surface in-situ measurements of methane and methyl-chloroform mole fractions are assimilated jointly for the period of 2002–2011. Compared to the prior simulation, the optimized CO concentrations show better agreement with independent surface in-situ measurements in terms of both distributions and trends. At the global scale, the atmospheric inversion primarily interprets the CO concentration decline as a decrease in the CO emissions, and finds noticeable trends neither in the chemical oxidation sources of CO, nor in the OH concentrations that regulate CO sinks. The latitudinal comparison of the model state with independent formaldehyde ($CH_2O$) columns retrieved from the Ozone Measurement Instrument (OMI) confirms the absence of large-scale trends in the atmospheric source of CO. The global CO emission decreased by 17 % during the decade, more than twice the negative trend estimated by emission inventories. The spatial distribution of the inferred decrease of CO emissions indicates contributions from both a decrease in fossil- and bio-fuel emissions over Europe, the USA and Asia, and from a decrease in biomass burning emissions in South America, Indonesia, Australia and Boreal regions. An emission decrease of 2 % $yr^{-1}$ is inferred in China, one of the main emitting regions, in contradiction with the bottom-up inventories that report an increase of 2 % $yr^{-1}$ during the study period. A large decrease in CO emission factors due to technology improvements would outweigh the increase of carbon fuel combustions and may explain the observed decrease. In Africa, instead of the negative trend





ACPD
15, 14505–14547, 2015



($1\,\%\,yr^{-1}$) reported by CO emission inventories mainly contributed by biomass burning, a positive trend ($1.5\,\%\,yr^{-1}$) is found by the atmospheric inversion, suggesting different trends between satellite-detected burned areas and CO emissions.

## 1 Introduction

Carbon monoxide (CO) is an air pollutant that leads to the formation of tropospheric ozone ($O_3$) and carbon dioxide ($CO_2$) (Jacob, 1999). It is the major sink of the tropospheric oxidant hydroxyl radical (OH), and hence influences concentrations of methane ($CH_4$) and non-methane volatile organic compounds (NMVOCs) (Logan et al., 1981). It contributes to an indirect positive radiative forcing of $0.23 \pm 0.07\,W\,m^{-2}$ at the global scale (Stocker et al., 2013). Atmospheric CO has two main sources: (i) direct surface CO emissions from fuel combustion and biomass burning, estimated to be $\sim 500$–$600\,TgCO\,yr^{-1}$ and $\sim 300$–$600\,TgCO\,yr^{-1}$, respectively, by emission inventories (Granier et al., 2011 and references herein), and (ii) secondary chemical oxidation of hydrocarbons in the troposphere, estimated to be a source of $\sim 1200$–$1650\,TgCO\,yr^{-1}$ with considerable differences among studies (Holloway et al., 2000; Pétron et al., 2004; Shindell et al., 2006; Duncan and Logan, 2008). The sink of CO is mainly through oxidation by OH (Logan et al., 1981), which defines an average lifetime of 2 months for CO in the atmosphere.

Surface in-situ measurements in Europe (Zellweger et al., 2009; Angelbratt et al., 2011), over the USA (Novelli et al., 2003; EPA, 2014), in some large cities in China (Li and Liu, 2011), and in many other places (Yoon and Pozzer, 2014) indicate that CO concentrations have been decreasing for more than ten years. Negative trends have also been observed by various satellite sensors (MOPITT, Technology Experiment Satellite – TES, and Atmospheric Infrared Sounder – AIRS) over most of the world (Worden et al., 2013). In particular, strong CO concentration decreases are seen from these satellite retrievals over East China and India (Worden et al., 2013), where bottom-up inventories report increasing emissions (Granier et al., 2011; Kurokawa et al., 2013).





ACPD
15, 14505–14547, 2015



The interpretation of trend differences or similarities between models and observations is made complicated by the fact that most atmospheric chemistry-transport models (CTMs) forced with current emission inventories underestimate CO concentrations in the mid to high latitudes of the Northern Hemisphere (NH), whereas they overestimate them over emission hotspots (Shindell et al., 2006; Duncan et al., 2007; Naik et al., 2013; Stein et al., 2014; Yoon and Pozzer, 2014). This bias reveals a wrong balance between CO sources, at the surface and in the atmosphere, and CO sinks (Naik et al., 2013). Understanding this model-data misfit is all the more so challenging that surface emissions and chemical production each account for about a half of the total CO sources, and that the sink term removes an amount of CO equivalent to all the sources within a few weeks. Changes in each source and sink term can contribute to the observed CO concentration decrease, even though only CO emission trends are usually discussed (Khalil and Rasmussen, 1988; Novelli et al., 2003; Duncan and Logan, 2008).

In principle, the attribution of the mean balance between sources and sinks and of their trends can be made with Bayesian inversion systems that infer the CO budget terms based on (i) measurements of CO and species related to the CO sources and sinks, (ii) some prior information about the budget terms and spatial distributions, (iii) a CTM model to link emissions, transport and chemistry to concentrations, and (iv) a description of the uncertainty in each information piece. Various inversion studies have estimated regional or global CO budgets using CO surface observations (Bergamaschi et al., 2000; Pétron, 2002; Butler et al., 2005) or satellites retrievals (Arellano et al., 2004; Pétron et al., 2004; Stavrakou and Müller, 2006; Chevallier et al., 2009; Fortems-Cheiney et al., 2009, 2011, 2012; Kopacz et al., 2010; Hooghiemstra et al., 2012a; Jiang et al., 2013). Here, we use the inversion system Python Variational – Simplified Atmospheric Chemistry (PYVAR-SACS) of Pison et al. (2009), Chevallier et al. (2009) and Fortems-Cheiney et al. (2009, 2011, 2012) to infer the origin of the observed CO concentration decrease in the past decade (2002–2011).





ACPD
15, 14505–14547, 2015



In contrast to most CO inversion systems cited above, which focused on a single species at once, PYVAR-SACS simultaneously assimilates observations of the main species in the chemical oxidation chain of $CH_4$-$CH_2O$-CO and methyl chloroform (MCF), a species that is chemically connected to hydrocarbons through its only reaction with OH. The PYVAR-SACS system optimizes the interconnected sources and sinks of the four species in a statistically and physically consistent way at the model resolution of $3.75^\circ \times 2.5^\circ$ (longitude, latitude) on an 8 day basis, therefore being suitable for addressing the above-described attribution problem of the CO variations within the limit of the observation information content.

The primary data source about CO in this study is MOPITT, a multi-channel thermal infrared (TIR) and near infrared (NIR) instrument on board the EOS-Terra satellite (Deeter, 2003). MOPITT provides the longest consistent time series of satellite CO retrievals to date. The algorithm has undergone continuous improvements and several re-processings of the archive have been made (Streets et al., 2013). Most of the above-cited satellite-based inversion studies used version 4 or earlier versions of the MOPITT CO retrievals, in which a noticeable instrumental drift was reported (Deeter et al., 2010). In version 5, this drift has been corrected together with other improvements (Deeter et al., 2013; Worden et al., 2013). Here, we use the further improved version 6, that has no noticeable bias in the trends of the CO total column (Deeter et al., 2014), to attribute the CO concentration decline by assimilation in our atmospheric inversion system.

The structure of the paper is as follows. Section 2 describes the inversion system and the datasets. Section 3 presents the inversion results on CO concentrations and associated trends. We show a brief evaluation of the inversion ability to fit the assimilated data and we cross evaluate the optimized surface CO concentrations against independent station measurements. Then, we compare the CO concentration trend in the MOPITT retrievals, in the surface measurements, and in corresponding modelling results before and after the inversion. Section 4 discusses the trends in the prior and the posterior simulated $CH_2O$ and OH concentrations. $CH_2O$ concentrations are rep-





ACPD
15, 14505–14547, 2015



resentative of the chemical CO sources and we evaluate the model values against retrievals of its dry air column ($X_{CH_2O}$) made from observations of Ozone Monitoring Instrument (OMI) aboard EOS Aura. OH regulates CO sinks, but is an extremely short-lived compound whose concentrations are difficult to measure (Mao et al., 2012). Lacking direct global observation data, we discuss its uncertainties with two contrasting prior OH fields. Section 5 presents the inverted CO budget, including atmospheric burden, emission, chemical production and chemical loss. Section 6 summarizes this work, discusses the sources of uncertainties and provides some perspectives for future works.

## 2 Method and data

### 2.1 Inversion system

The PYVAR Bayesian inversion system, initially introduced by Chevallier et al. (2005), aims at adjusting a series of target variables (jointly called $\boldsymbol{x}$), so that they become consistent with both the atmospheric observations ($\boldsymbol{y}$) and a priori state ($\boldsymbol{x}^{\mathrm{b}}$) given their respective uncertainties, represented by error covariance matrices $\mathbf{R}$ and $\mathbf{B}$. By iteratively minimizing the following cost function $J$, PYVAR finds the optimal solution for $\boldsymbol{x}$ in a statistical sense:

$$J(\boldsymbol{x}) = \frac{1}{2}(\boldsymbol{x} - \boldsymbol{x}^{\mathrm{b}})^{\mathrm{T}}\mathbf{B}^{-1}(\boldsymbol{x} - \boldsymbol{x}^{\mathrm{b}}) + \frac{1}{2}(H(\boldsymbol{x}) - \boldsymbol{y})^{\mathrm{T}}\mathbf{R}^{-1}(H(\boldsymbol{x}) - \boldsymbol{y})$$

where $H$ is the combination of a CTM and an interpolation operator that includes the integration of the retrieval prior CO profiles and averaging kernels (AKs) for MOPITT.

Our CTM is the general circulation model of Laboratoire de Météorologie Dynamique (LMDz) version 4 (Hourdin et al., 2006), nudged towards winds analysed by the European Centre for Medium-Range Weather Forecasts, run in an off-line mode with precomputed atmospheric mass fluxes, and coupled with the chemistry module SACS





ACPD
15, 14505–14547, 2015



(Pison et al., 2009). SACS is a simplification of the full chemistry model Interaction with Chemistry and Aerosols (INCA, Hauglustaine, 2004).

The chemical chain is shown in Fig. 1. It includes surface emissions of CO, $CH_4$, $CH_2O$ and MCF. The 3-D contribution of NMVOCs oxidation to $CH_2O$ production has been pre-calculated by the full chemistry transport model LMDz-INCA (Folberth et al., 2006). OH links all the species together, and the effects of $NO_x$ are not considered. Reaction kinetic and photolysis rates, as well as fields of species that are not represented as tracers in PYVAR-SACS (e.g. $O_1D$, $O_2$, Cl) are based on LMDz-INCA. The CTM in PYVAR-SACS has a time step of 15 min for the dynamics (advection) and of 30 min for the physics (convection, boundary layer turbulence) and chemistry, a horizontal resolution of 3.75° × 2.5° (longitude, latitude), and a vertical resolution of 19 eta-pressure levels from the surface to the top of the atmosphere.

The state vector $\boldsymbol{x}$ contains the following variables as shown in the grey boxes in Fig. 1: (1) grid-point scaling factors for the initial pressure-weighted column-mean concentrations of the four trace gas species (CO, $CH_4$, $CH_2O$, MCF), (2) grid-point 8 day mean surface emissions of CO, $CH_4$, and MCF, (3) grid-point 8 day scaling factors to adjust the pressure-weighted column-mean atmospheric $CH_2O$ production from NMVOCs, (4) 8 day scaling factors to adjust the pressure-weighted column-mean OH concentrations over 6 big boxes of the atmosphere over the globe: 3 latitudinal boxes (30–90° S, 0–30° S, 0–30° N) and 3 longitudinal boxes for the latitudes north of 30° N (NA: 180–45° W, EU: 45° W–60° E, Asia: 60–180° E). The longitudinal division of the band north of 30° N is an improvement compared to previous PYVAR studies (4 latitudinal bands in total) as it allows adjusting separately continental differences in OH.

## 2.2 A priori information

Previous configurations of PYVAR-SACS have been described by Chevallier et al. (2009) and Fortems-Cheiney et al. (2011). We have improved the configuration described below.





ACPD
15, 14505–14547, 2015



### 2.2.1 Prior sources and sinks

For prior anthropogenic fossil fuel and biofuel CO emissions, we use the monthly MACCity emission inventory of Lamarque et al. (2010) that arguably underestimates emissions less than other global inventories (Granier et al., 2011; Stein et al., 2014). For biomass burning, we update the version of Global Fire Emissions (GFED) from 2 (van der Werf et al., 2006) to 3.1 (Van der Werf et al., 2010). The latter has various improvements including the definition of different fire types, with specific consideration for deforestation and peatland fires. Additionally, we consider in this study biochemical CO emissions from oceans, that were neglected before, based on an ocean biogeochemical model simulation (Aumont and Bopp, 2006). These monthly ocean CO fluxes add up to a global annual sum of 54 $TgCO\,yr^{-1}$, for which the inter-annual variability is not considered in the prior. We still consider neither biogenic CO emissions over land, nor surface CO deposition, because these two terms are relatively small and are of a similar order (Duncan et al., 2007). The prior CO emissions are summarised in Table 1 and the distribution of the mean annual prior CO surface emissions is shown in Fig. 2a. The relative contribution of biomass burning is shown in Fig. 2b.

The prior $CH_4$ and MCF emissions have also been updated compared to Fortems-Cheiney et al. (2012) and are similar to that of Cressot et al. (2014). 3-D HCHO production prior fields have been pre-calculated by LMDz-INCA (Folberth et al., 2006), with prescribed NMVOC emission datasets detailed in Fortems-Cheiney et al. (2012). The prior distribution of mean annual CO chemical sources in the troposphere from the oxidation of both $CH_4$ and NMVOCs are shown vertically integrated in Fig. 2c.

Previous PYVAR-SACS studies used prior OH information from a multi-year simulation by LMDz-INCA (Hauglustaine, 2004). Here, we use another field that was prepared for the international TransCom-$CH_4$ experiment of Patra et al. (2011). We call this field TransCom-OH. It has a north–south inter-hemisphere ratio of 1, whereas the INCA-OH has a ratio of 1.2. There are also vertical differences between these two OH-fields: TransCom-OH has considerably higher OH concentrations over the top lay-





ACPD
15, 14505–14547, 2015



ers above 100 hPa, whereas INCA-OH has slightly higher OH concentrations in the lower troposphere below 800 hPa. The prior distribution of the CO sinks prescribed with TransCom-OH is shown vertically integrated in Fig. 2d.

### 2.2.2 Prior error statistics

The prior flux uncertainty, defined by the standard deviation (SD) of each grid-point 8 day flux, is described below. For CO emission uncertainties, we define the SD for each year based on the maximum value of the emission time series during the corresponding year for each grid point (noted as $f_{max}$), in order to account for the uncertainty of the fire timing. Then, to account for (i) the possibility of undetected small fires that can contribute to as much as 35 % of the global biomass burning carbon emissions (Randerson et al., 2012), and (ii) potentially higher CO emission factors during small fires that were not specifically considered in current fire emission inventories (Leeuwen et al., 2013), we define a fire emission threshold of $1.0 \times 10^{-10}$ kg CO m$^2$ s$^{-1}$. If the prior emission is less than the threshold (no fire a priori, but there could be one in reality), the SD is set as 100 % of $f_{max}$. Otherwise (fire a priori, but possibly of a too small magnitude), the SD is set as the maximum value between $1.0 \times 10^{-9}$ kg CO m$^2$ s$^{-1}$ and 50 % of $f_{max}$. In such a way, we allow the system to relax the constraint on the prior emission to account for undetected emissions, but we keep the global uncertainty ($\sim 180$ TgCO yr$^{-1}$) consistent with current bottom-up inventories (Granier et al., 2011; Van der Werf et al., 2010). For simplicity, this error setting also serves for anthropogenic fuel consumption.

The prior $CH_4$ emission uncertainty is defined as 100 % of the maximum value of the prior emissions in the grid cell and its eight neighbours in the corresponding month. The MCF prior emission uncertainty is set at ±10 % of the flux, as its emissions are supposed to be well known. The uncertainty of $CH_2O$ production is assumed to be 100 % of its concurrent prior $CH_2O$ production. The uncertainties of initial concentration scaling factors are set at 10 % for the four species (CO, $CH_4$, $CH_2O$, MCF). Errors on OH 8 day scaling factors are set at ±5 %.





ACPD
15, 14505–14547, 2015



The spatial error correlations of the a priori are assigned to all variables following Chevallier et al. (2007), defined by an e-folding length of 500 km over the land and 1000 km over the ocean. Temporal error correlations are defined by an e-folding length of 8 weeks for MCF and 2 weeks for the other species including OH. No inter-species flux error correlations are considered.

## 2.3 Observations for assimilation

### 2.3.1 Datasets

We assimilate three data streams: (i) MOPITTv6 satellite CO total column retrievals (noted as $X_{CO}$ hereafter) and surface in-situ measurements of (ii) $CH_4$ and (iii) MCF.

MOPITT retrievals are available since March 2000, but the instrument experienced a cooler failure from May 2001 to August 2001, which artificially changed the retrieval mean level (Deeter et al., 2010). An instrument anomaly also led to a 2 month lack of data in 2009 from the end of July until September, without any significant change in the retrieval mean level. For the sake of consistency, given our focus on trends, we select the measurements for the decade from 2002 to 2011, during which both the MOPITT retrievals and the prior emission inventories are homogeneous (GFEDv3.1 has not been publicly updated for the years after 2011).

We use the level 2 "multispectral" near and thermal infrared (NIR/TIR) CO retrievals of MOPITTv6 that offer the best description of CO in the lower troposphere among the MOPITT products (Deeter et al., 2014). The MOPITT vertical profiles (prior and retrieved CO profiles and associated AKs) are defined on ten vertical pressure levels. Given the limited vertical resolution of the retrievals and the focus on surface emissions, it has been common practice in previous inversion studies starting from Pétron et al. (2004) to assimilate the 700 hPa pressure level retrievals only, as a good compromise between proximity to the surface and limited noise. However, Deeter et al. (2014) noted that the retrievals at some individual vertical levels still suffered from small bias drifts while such drifts were not seen in the retrieved integrated columns. Furthermore,





ACPD
15, 14505–14547, 2015



the interpretation of vertically-integrated columns in the inversion is less hampered by flaws in CTM vertical mixing and vertical sink distribution than for level retrievals (Rayner and O'Brien, 2001). For these two reasons, we assimilate the column retrievals $X_{CO}$ (with their original prior CO profiles and AKs) rather than level retrievals. Night-time observations, observations with solar zenith angle larger than 70°, with latitudes within 25° from the poles, or with surface pressures less than 900 hPa are excluded, since they may be of lower quality or more difficult to model. We average the 22 km × 22 km retrievals at the 3.75° × 2.5° model resolution within 30 min time steps.

Surface measurements of $CH_4$ and MCF from various networks are assimilated together with MOPITT $X_{CO}$. The datasets are downloaded from the World Data Centre for Greenhouse Gases (WDCGG, http://ds.data.jma.go.jp/gmd/wdcgg/). Stations that recorded more than 6 years of data without gaps larger than 1 year are included. The list of stations is given in Tables S1 and S2. For the surface measurements, a data filtering process is conducted in order to remove outliers that the global model may not be able to capture. We exclude (i) observations exceeding $3\sigma$ of the de-trended and de-seasonalized daily time series and (ii) observations whose misfit against the prior simulation exceeds $3\sigma$ of the de-trended and de-seasonalized misfit between observations and forward modelling values.

### 2.3.2 Observation error statistics

The observation error covariance matrix **R** is diagonal in order to simplify calculations. Observation errors are combinations of measurement errors (quantified by the data providers), representativeness errors and CTM errors. For $X_{CO}$, as we have averaged a large amount of observations in each grid-box (see Sect. 2.3.2), the representativeness error is effectively much reduced and is not considered specifically. The CTM error is set at 30 % (SD) of the modelled values for $X_{CO}$. For $CH_4$ and MCF, the yearly means of synoptic variability is used as a proxy for the CTM and representativeness errors, which largely dominate the observation error.





ACPD
15, 14505–14547, 2015



## 2.4 Observations for cross evaluation

We use two datasets for independent evaluation of the inversion results.

The first one is made of CO surface observations archived at the WDCGG. The same site selection and data filtering process as for $CH_4$ and MCF surface measurements are applied (see the list of stations in Table S3).

The second evaluation dataset gathers $CH_2O$ total columns retrieved from OMI by the Smithsonian Astrophysical Observatory (SAO). We use version 3, release 2, of this product (González Abad et al., 2015). Since this data is not available before mid-2004, it does not cover our study period completely: for the sake of consistency, we do not assimilate it (in contrast to Fortems-Cheiney et al., 2012) and we keep it for evaluation. We select observations that are tagged as "good" by the provider's quality flag, which have a solar zenith angle less than 70°, a cloud cover below 20 %, and are not affected by the "row anomaly".

## 2.5 Trend analysis

The long-term trend in this study is estimated by least-square curve fitting of the following function, which includes a constant, a linear component, and seasonal variations represented by four harmonics:

$$f(t) = a_0 + a_1 t + \sum_{n=1}^{4} c_n[\sin(2n\pi t + \varphi_n)]$$

If not particularly specified, all the trends mentioned in this paper refer to $a_1$.





ACPD
15, 14505–14547, 2015



## 3 CO concentrations and associated trends

### 3.1 Evaluation of the inversion framework's ability to fit the data

The time series of global mean $X_{CO}$ from MOPITT observations (black) is shown for the period from September 2001 to October 2014 in Fig. 3a, and the prior (green) and the posterior (red) assimilations are shown for the period from 2002 to 2011, with four months in 2001 for spin up. Compared to the MOPITT $X_{CO}$, the prior $X_{CO}$ simulation is on average 15 % lower with TransCom-OH and 17 % lower with INCA-OH. The global mean posterior CO concentrations fit the observation whatever the OH field used.

Figure 3b presents the map of the multiyear mean $X_{CO}$ observed by MOPITT (2002–2011). It shows a latitudinal gradient from north ($2.14 \pm 0.19 \times 10^{18}$ molec cm$^{-2}$ between 30–60° N) to south ($1.16 \pm 0.09 \times 10^{18}$ molec cm$^{-2}$ between 30–60° S), with high values over East Asia ($2.5 \pm 0.4 \times 10^{18}$ molec cm$^{-2}$), Africa ($1.95 \pm 0.3 \times 10^{18}$ molec cm$^{-2}$) and central South America ($1.8 \pm 0.1 \times 10^{18}$ molec cm$^{-2}$) (Fig. 3b). The prior simulation is generally lower ($-0.24 \pm 0.1 \times 10^{18}$ molec cm$^{-2}$) than the observations except in parts of Indonesia and India (Fig. 3c). This negative bias agrees with previous studies (Arellano et al., 2004; Fortems-Cheiney et al., 2011; Hooghiemstra et al., 2012a, Naik et al., 2013; Shindell et al., 2006), and thus calls attention to understanding and correcting it appropriately (Stein et al., 2014). The optimized CO concentrations fit the measurements better (Fig. 3d), illustrating the inversion ability to fit the data. Similarly for $CH_4$ and MCF, the inversion fits the assimilated data fairly well, but these results are not shown, as they are not the main focus in this study.

Compared to the independent surface in-situ CO measurements, the optimized CO concentrations better fit the observations in terms of both mean values and trends (Fig. 4). The magnitude of the model-data misfits after optimization is considerably reduced compared to the prior model-data misfits. The magnitude of posterior misfits is decreased by 61 % (19.4 ppb) in the NH – North of 30° N (Fig. 4a), by 72 % (12.7 ppb) in the NH-Tropics (Fig. 4b) and by 62 % (9.2 ppb) in the SH-Tropics (Fig. 4c). The





ACPD
15, 14505–14547, 2015



posterior misfit in the Southern Hemisphere (SH) – South of 30° S is of a similar magnitude (7.3 ppb) to the prior misfit (−7.7 ppb), but the sign changed from negative to positive (Fig. 4d). While the prior model-data misfits are mostly negative, the posterior misfits generally show small positive signs, especially over the SH mid-high latitudes. Two factors might have contributed to the differences: firstly the total column sensitivity of satellite retrievals may not inform well enough about the CO concentration in the boundary layer as seen by surface observations (Hooghiemstra et al., 2012), and secondly there might be a model bias in modelling vertical CO profiles in CTMs (Jiang et al., 2013).

Significant trends are seen in the prior misfits but are corrected in the posterior misfits (Fig. 4). For instance, positive trends in the prior misfits were present in the NH ($0.67 \pm 0.24\,\mathrm{ppb\,yr^{-1}}$) and NH-Tropics ($0.66 \pm 0.14\,\mathrm{ppb\,yr^{-1}}$), and they are changed to smaller negative trends of $-0.48 \pm 0.15\,\mathrm{ppb\,yr^{-1}}$ in the NH and non-significant in the NH-Tropics after assimilation (Fig. 4a and b). Such trends in the posterior misfits are within the uncertainty ranges of the trends in the observations ($-2.5 \pm 0.6\,\mathrm{ppb\,yr^{-1}}$ in the NH and $-1.1 \pm 0.4\,\mathrm{ppb\,yr^{-1}}$ in the NH-Tropics). Negative trend in the prior misfit of $-0.42 \pm 0.14\,\mathrm{ppb\,yr^{-1}}$ is seen in the SH-Tropics where no significant trend is found in the latitudinal mean concentration, and the trends in prior misfits are corrected after assimilation (Fig. 4c).

### 3.2 Distribution of trends in CO concentrations

The spatial distribution of trends in CO concentrations from 2002 to 2011 is shown in Fig. 5. The upper row successively shows the trends in $X_{CO}$ from the MOPITTv6 retrievals, from the prior simulation and from the posterior simulation; similarly, the lower row shows the trends in CO concentrations at the surface in-situ stations from WDCGG and corresponding prior/posterior trends sampled at those sites.

MOPITT $X_{CO}$ retrievals show negative trends in most regions of the world except for the Sahel region in Africa and some areas of central South America and India (Fig. 5a). The global average trend is $-1.5 \pm 0.8 \times 10^{16}\,\mathrm{molec\,cm^{-2}\,yr^{-1}}$, ac-





ACPD
15, 14505–14547, 2015



counting for a decrease of around 1 % $yr^{-1}$ over the globe. The negative trends are particularly large over Indonesia ($-3.0 \pm 1.1 \times 10^{16}$ molec $cm^{-2}$ $yr^{-1}$), South East Asia ($-2.5 \pm 0.9 \times 10^{16}$ molec $cm^{-2}$ $yr^{-1}$) and the Northern Pacific and Atlantic Ocean ($-2.6 \pm 0.3 \times 10^{16}$ molec $cm^{-2}$ $yr^{-1}$). In general, the surface stations also present negative CO concentration trends (Fig. 5d). The negative trend from in-situ CO stations has the largest magnitude in the NH mid-latitudes over Europe ($-2.9 \pm 1.7$ ppb $yr^{-1}$) and the USA ($-1.6 \pm 0.9$ ppb $yr^{-1}$). Smaller trends are found in the SH in-situ sites ($-0.32 \pm 0.14$ ppb $yr^{-1}$). The trends over Asia indicate large spatial heterogeneity ($-1.6 \pm 1.3$ ppb $yr^{-1}$) and the trends over the Tropics show a small increase ($0.3 \pm 1.6$ ppb $yr^{-1}$), but these regions are represented by a limited number of stations that are sparsely distributed.

In the prior simulation, the CO columns, vertically integrated with the MOPITT retrieval prior profile and AK (Fig. 5b), present small negative trends in most regions of the NH except for China. Positive trends are simulated over South America and South Africa. The global average prior simulated CO trend is $-0.3 \pm 0.38 \times 10^{16}$ molec $cm^{-2}$ $yr^{-1}$. Such trends are not very consistent with the MOPITT observed $X_{CO}$ trends, except over Europe ($-1.4 \pm 0.2 \times 10^{16}$ molec $cm^{-2}$ $yr^{-1}$) and the USA ($-1.1 \pm 0.38 \times 10^{16}$ molec $cm^{-2}$ $yr^{-1}$), where the prior modelled CO trends are comparable with but of smaller amplitudes than the trends in MOPITT observations. As for the surface stations (Fig. 5e), the prior simulation trends in Europe ($-3.0 \pm 1.1$ ppb $yr^{-1}$) and the USA ($-1.8 \pm 1.0$ ppb $yr^{-1}$) agree roughly with the observations, but the prior simulation trends over Asia ($-1.5 \pm 1.8$ ppb $yr^{-1}$) and the Tropics ($-0.6 \pm 2.5$ ppb $yr^{-1}$) are different from the trends in the surface observations. The positive trends in the prior simulated $X_{CO}$ (Fig. 5b) are more pronounced than those of the prior simulated surface CO (Fig. 5e), given the respective vertical weighting of these two observation types. In addition, such difference may also be enhanced by changes in the MOPITT AKs if the retrieval prior is biased (Yoon et al., 2013). However, stations in these two regions are relatively sparse and may not be representative for regional trends compared to satellite retrievals.





ACPD
15, 14505–14547, 2015



In the posterior simulation (sampled the same way as the prior simulation with the MOPITT AKs), a general decreasing trend appears with the same distribution as in the assimilated satellite observations (compare Fig. 5c and a). When the posterior simulation is sampled at the surface stations, which were not used in the inversion (Fig. 5f), most locations show similar negative trends as the trends in observations. As described in Sect. 3.1 (Fig. 4), the discrepancies in the trends between our prior simulation and the observations at the surface stations are corrected in our posterior simulation.

## 4 Concentrations of $CH_2O$ and OH

### 4.1 $CH_2O$ concentrations

The mean time series of $CH_2O$ total columns for the four latitudinal zones are shown in Fig. 6. $X_{CH_2O}$ retrievals were not assimilated (contrary to the $CH_4$ and MCF surface measurements that affect the source and sinks of $CH_2O$ in the inversion), and the inversion actually does not change $X_{CH_2O}$ much. This suggests that the differences between simulated and satellite-retrieved $X_{CH_2O}$ are mainly caused by the prior NMVOC emissions used in the full chemistry run of LMDz-INCA. The latitudinal mean values of prior/posterior modelled $X_{CH_2O}$ fairly agree with the OMI retrievals without any obvious bias, but the seasonal cycle is different especially in the Northern mid-high latitudes both in phase and in amplitude (Fig. 6a). The OMI $X_{CH_2O}$ retrievals, the prior and the posterior simulations all agree about the absence of trend in the latitudinal average of $X_{CH_2O}$ for the period from 2005 to 2011, which is consistent with the hypothesis that the equilibrium between the oxidation of hydrocarbons into $CH_2O$ and the sink of $CH_2O$ into CO has not significantly changed, at least at continental scales. We note that the OMI $X_{CH_2O}$ retrievals describe some trends at smaller scales, like positive trends of $3 \pm 0.8\,\%\,yr^{-1}$ over East Asia (De Smedt et al., 2010) and negative trends of





ACPD
15, 14505–14547, 2015



$-1.9 \pm 0.6\,\%\,yr^{-1}$ over the Amazon, but they cancel each out on the latitudinal means and are thus considered not large enough to influence the global CO budget.

### 4.2 OH concentrations

Figure 7 shows the latitudinal average of the prescribed (dashed lines) and optimized (solid lines) OH concentrations (total column) for the 6 big regions over which OH is optimized (see Sect. 2.1). This figure reports the two inversions that use either TransCom-OH (in red) or INCA-OH (in green; see Sect. 2.2.1). INCA-OH has higher than TransCom OH concentrations in the NH during summer OH maximum, but lower than TransCOm OH concentrations in the SH Tropics all year long and slightly lower concentrations in the SH mid-high latitudes (South of 30° S) during summer peaks.

In general, larger corrections are applied by the inversion to INCA-OH than to TransCom-OH. The inversion system adjusts the INCA-OH concentrations towards TransCom-OH by downscaling the OH concentrations in the NH during summers, especially over Asia, where INCA-OH is considerably higher than the TransCom-OH (Fig. 7). A small reduction of the TransCom-OH concentrations is also seen in the SH.

The two inversions do not produce significant trends in OH during the study period for most regions, except for a very small positive trend in the SH Tropics ($+0.2\,\%\,yr^{-1}$ with TransCom-OH and $+0.7\,\%\,yr^{-1}$ with INCA-OH) and a small negative trend in the SH mid-high latitudes ($-0.4\,\%\,yr^{-1}$ in TransCom-OH and $-0.3\,\%\,yr^{-1}$ in INCA-OH). Such small trends are considered of minor effect on the CO trends. The OH scaling is addressed more in details in Sect. 5.1 when discussing CO sinks.

## 5 Optimized sources and sinks of CO

After having documented the prior and the posterior misfits with MOPITTv6 and with cross validation data for the latitudinal mean values and for the trends, which lends





ACPD
15, 14505–14547, 2015



support to the consistency of the inversion results with these data-streams, we now turn to the implications for CO sources and sinks.

### 5.1 Inverted CO budget

The global annual CO atmospheric burden, surface emissions, chemical production, and chemical loss from 2002 to 2011 are shown in Fig. 8. The dashed lines present the prior budget and the solid lines the posterior budget in each term; the shaded areas around the solid lines indicate the SD between the two OH experiments. Averaging over the 10 years, a considerable increase of the mean CO atmospheric burden (+24 %, in dark green) is seen in the posterior compared to the prior simulation. Accordingly, increases of CO emissions (+39 %, in red) and chemical sinks with OH (+17 %, in purple) are produced in the posterior, whereas only a very small change is noticed for the CO chemical sources (−3 %, in blue). The chemical CO source here is calculated from the oxidation of $CH_4$ and $CH_2O$ (indirectly from NMVOCs), whose concentration fields generally agree with independent observations as shown above in Sect. 4.1. The chemical sink of CO is a function of both CO and OH. Given the results for OH adjustments shown in Sect. 4.2 (generally small reduction from the prior OH), the increase of the CO sink in the posterior is thus mainly due to the increase of CO concentrations after assimilation.

The inversion produces a negative trend of $-4.8 \pm 0.8\,\mathrm{TgCO\,yr^{-1}}$ in the global atmospheric burden of CO (equivalent to a decrease of $10\,\%\,\mathrm{decade^{-1}}$), which is twice the negative trend produced by the prior emissions ($-1.8 \pm 0.6\,\mathrm{TgCO\,yr^{-1}}$, i.e. a decrease of $5\,\%\,\mathrm{decade^{-1}}$ in the simulated CO burden). These trends are calculated from the mean results of TransCom-OH and INCA-OH inversions and uncertainties noted here represent the uncertainty of the regression.

For CO sources, the trend of prior CO emissions is of $-11.4 \pm 3.6\,\mathrm{TgCO\,yr^{-1}}$ (equivalent to a decrease of $10\,\%\,\mathrm{decade^{-1}}$). This is mostly contributed by the negative trend in biomass burning emissions in GFEDv3.1 ($-10.6 \pm 3.7\,\mathrm{TgCO\,yr^{-1}}$) and by a very small decrease in anthropogenic emissions in MACCity ($-0.68 \pm 0.4\,\mathrm{TgCO\,yr^{-1}}$) from 2002





ACPD
15, 14505–14547, 2015



to 2009. Compared to the prior emissions, a two-fold more negative trend is found in the posterior CO emissions, $-26.1 \pm 4.5\,\mathrm{TgCO\,yr^{-1}}$ ($17\,\%\,\mathrm{decade^{-1}}$). The trends in both the prior and the posterior CO chemical productions are small and not statistically significant.

For the CO sink, a larger trend in the posterior ($-28.9 \pm 5.3\,\mathrm{TgCO\,yr^{-1}}$, $10\,\%\,\mathrm{decade^{-1}}$) is found compared to the prior simulation ($-11.0 \pm 3.6\,\mathrm{TgCO\,yr^{-1}}$, $4.8\,\%\,\mathrm{decade^{-1}}$). This trend is mostly due to the decrease of CO concentrations in the atmosphere that change the amount of CO oxidized by OH at each time step, and no significant trend in the OH concentrations are found by the inversion. Yet, the OH concentrations are optimized for 6 big regions over the globe and the MCF observation are monitored at background sites only, which allows a coarse zonal estimate of OH but leaves spatially heterogeneous land areas unconstrained, e.g. polluted areas near cities (Hofzumahaus et al., 2009), forests with high NMVOC emissions (Lelieveld et al., 2008) or biomass burning plumes (Folkins et al., 1997; Rohrer et al., 2014). Therefore, sub-regional trends in OH, if they exist, are not necessarily captured in this study. In addition, with the exponential decrease of MCF concentrations in recent years (only a few parts per trillion, ppt, at the current level), the constraining strength of MCF on OH in the inversion system may not be even from 2002 to 2011, even though the same sites and a similar number of observations were assimilated. Nevertheless, the zonal trend of OH should still be constrained throughout most of the period and previous studies suggest that the inter-annual change of global OH concentration is within 5 % and bears no significant trend for the period from 1998 to 2007 (Montzka et al., 2011).

### 5.2 Regional distribution of trends in CO emissions

The trends in CO emissions after optimization are consistent using either TransCom-OH or INCA-OH; therefore, only results of the assimilation using TransCom-OH are discussed here. The distributions of trends in the prior and the posterior CO emissions over the globe are shown in Fig. 9. The relative contribution of biomass burning to the total land surface emissions estimated by the prior emission is shown in Fig. 2b. The





ACPD
15, 14505–14547, 2015



time series of the prior and the posterior annual CO emissions for each sub-region are shown in Fig. 10 and the division in sub-regions is illustrated in Appendix Fig. A1. For the boreal regions where CO emissions are mainly due to biomass burning (Boreal Asia – BOAS and Boreal North America – BONA), the same sign of the trends in CO emissions is mostly kept between the prior and the posterior, but the amplitude of the trends are updated into larger values, so are the emission amounts.

For the NH mid-latitudes where CO emissions are mainly due to fossil fuel and biofuel burning emissions (USA, West Europe – WSEU, East Europe – ESEU, Middle East – MIDE, South Central Asia – SCAS, South East Asia – SEAS), consistencies between the trends in the prior and the posterior CO emissions are found in the developed countries (Fig. 9). For example in the USA and WSEU regions, decreasing trends produced by the emission inventories generally agree with the atmospheric signals (Lamarque et al., 2010). On the contrary, the inversion changes the sign of the CO trend over SEAS (including China) and SCAS (including India), where the prior emissions suggest an increase. Consistent with our posterior emissions, a gradual decrease of CO emissions in China after the year 2005 was actually deduced from $CH_4/CO_2$ and $CO/CO_2$ correlations observed off the coast of East Asia from 1999–2010 (Tohjima et al., 2014). A decrease of the emission factors of other co-emitted species of CO during fossil fuel or biofuel combustion has also been noted: for instance, a decrease of black carbon emission factors in China and India was reported by Wang et al. (2014), and a decrease in the relative ratio of $NO_x$ to $CO_2$ from 2003 to 2011 was observed from satellite retrievals over East Asia (Reuter et al., 2014). These studies and our results suggest that combustion technology improvements in East Asia resulted in emission factor reduction to an extent that outweighs the impact of increasing fossil fuel burning. In this scenario, emission inventories would well report the latter but not the former that is more difficult to quantify. In addition, trends of fossil fuel emissions are updated (Lamarque et al., 2010) but not trends of biofuel burning, especially for traditional biofuels (Yevich and Logan, 2003). A small difference in the changing rate of CO emissions in East Europe





ACPD
15, 14505–14547, 2015



(ESEU) is also noticed, with much higher emissions in the year 2010 than estimated in the prior.

For the tropical and sub-tropical regions, where CO emissions are mainly contributed by biomass burning, the inversion does not change the sign of trends in most regions of Southern Hemisphere South America (SHSA), Indonesia (INDO) and Australia (AUST), though the amplitude of the trends changes (Fig. 9). For instance, the inversion produces larger negative trends over SHSA than the prior. A significant decreasing trend in SHSA is observed in the burned area, in agreement with the new version of GFEDv4 burned area (not used in this study) (Giglio et al., 2013), which accounts for small fires that were not explicitly included in GFEDv3.1 used here as the prior. This decrease could be attributed to a decrease of deforestation fires in recent years, especially after 2005 (Meyfroidt and Lambin, 2011), although there are uncertainties in the overall deforestation rates (Kim et al., 2015).

The change in trends between the prior and the posterior CO emissions is large over Africa (Northern Hemisphere Africa – NHAF and Southern Hemisphere Africa – SHAF). Decreases in the burned area have been observed over the NHAF Sahel region, so are decreases in the prior CO emissions, which are explained by changes in both precipitation and the conversion of savannah into cropland (Andela and van der Werf, 2014). On the contrary in our study, positive trends in CO emissions are infered by the atmospheric inversion, except for a small region in Cameroon. The different signs of the trend in burned area (or the prior CO emissions) and the posterior CO emissions may be explained by the change in CO emission factors that could vary a lot with the conversion of fire type from savannah fire to agricultural burning and also with precipitation change (van Leeuwen et al., 2013). In addition, increases of anthropogenic fossil fuel and biofuel emission in the NHAF region could also contribute to some of the differences (Al-mulali and Binti Che Sab, 2012). Differences between the prior and the posterior CO emissions are also noticed for the central part of the SHAF. The increase in the GFED4 burned area is explained by the increase of precipitation that allows more fuel accumulation, as driven by the El Niño/Southern Oscillation (ENSO) changes from





ACPD
15, 14505–14547, 2015



El Niño to La Niña dominance over the recent decade (Andela and van der Werf, 2014). The opposite negative trend of CO emissions in the posterior could be explained by a decrease in CO emission factors when the fuel load and combustion completeness are high so that less carbon is emitted in the form of CO; but the dynamics of emission factors are not modelled in the bottom-up estimation (van Leeuwen et al., 2013). In addition, small fires that are not considered in our prior biomass emissions could also contribute to such differences (Randerson et al., 2012).

## 6 Conclusions

CO concentrations observed by both MOPITTv6 satellite $X_{CO}$ retrievals and surface in-situ measurements show significant negative trends over most of the world from 2002 to 2011. Such decreasing trends have continued until the end of 2014 according to the latest MOPITT observations. The CO concentration trends in the forward CTM simulations prescribed with CO emission inventories show considerable inconsistency with the observed MOPITT $X_{CO}$. By assimilating MOPITTv6 $X_{CO}$ and surface measurements of $CH_4$ and MCF, the inversion system suggests that the decrease in the atmospheric CO concentrations is mainly attributable to a decrease of 17 % in surface emissions during the study period at the global scale. The inverted global annual emission has decreased from 1506 to 1235 $TgCO\,yr^{-1}$, during the decade when simulated with our reference OH field (TransCom-OH). The trends in the prior and the posterior CO emissions agree well with each other over the USA and Western Europe. The largest differences between the prior and the posterior CO emission trends are noticed for Asia and Africa. Decreases of CO emissions are found in parts of China and India, whereas the prior emission suggests increases. This emission decrease is probably caused by a large decrease of emission factors due to technology improvements that outweigh the increase of emission activities. For Africa, large changes in the trends likely reflect different trends between satellite-detected burned area and CO emissions due to changes in combustion completeness, CO emission factors, and the relative





ACPD
15, 14505–14547, 2015



contribution of small fires. The amplitude of the trends also differs in many other regions, illustrating the original information brought by atmospheric inversions about CO emissions.

No significant trend is found in the latitudinal-mean OH concentrations, and a sensitivity test made with two different OH fields suggests consistent results in the OH trend. Sub-regional trends in the OH concentrations, if they exist, are not accounted for in this study because we optimize it in six big regions only. We also acknowledge the limited information content of MCF to constrain OH over the study period. For chemical $CH_2O$ production from NMVOC oxidation, the system has the potential to generate regional increments, but $CH_2O$ is not assimilated here due to limited temporal coverage of the OMI data from 2005 to 2011. No noticeable trend for this period is observed in the latitudinal mean $CH_2O$ concentrations, which are representative of the equilibrium between the oxidation of hydrocarbons into $CH_2O$ and the sink of $CH_2O$ into CO. It is however noted that some small regional trends in $X_{CH_2O}$ are missed by the inversion. These unconstrained sub-regional trends in OH and $CH_2O$ suggest assimilating observations from other connected species to increase the constraints on each term of the CO budgets in future studies.

**The Supplement related to this article is available online at doi:10.5194/acpd-15-14505-2015-supplement.**

*Acknowledgements.* The authors acknowledge the support of the French Agence Nationale de la Recherche (ANR) under grant ANR-10-BLAN-0611 (project TropFire). F. Chevallier is funded by the European Commission under the EU H2020 Programme (grant agreement No. 630 080, MACC III). The NCAR MOPITT and the SAO OMI retrievals are available from https://www2.acd.ucar.edu/mopitt and http://disc.sci.gsfc.nasa.gov/Aura/data-holdings/OMI/omhcho_v003.shtml, respectively. We thank both institutes for having brought this data into open access and thank G. González Abad for helpful information about the OMI product. Similarly, we also acknowledge the WDCGG for providing the archives of surface station observations for





ACPD
15, 14505–14547, 2015



MCF, $CH_4$ and CO. We thank the following persons who have participated to the surface in-situ measurements through various networks: NOAA (E. Dlugokencky, G. S. Dutton, J. W. Elkins, S. A. Montzka, P. C. Novelli), CSIRO (P. B. Krummel, R. L. Langenfelds, L. P. Steele), EC (D. Worthy), Empa (B. Buchmann, M. Steinbacher, L. Emmenegger), JMA (Y. Fukuyama), LSCE (M. Ramonet), NIWA (G. Brailsford, S. Nichol, R. Spoor), UBA (K. Uhse), UNIURB (J. Arduini), and AGAGE (P. J. Fraser, C.M. Harth, P. B. Krummel, S. O'Doherty, R. Prinn, S. Reimann, L. P. Steele, M. Vollmer, R. Wang, R. Weiss, D. Young). Finally, we wish to thank F. Marabelle and his team for computer support at LSCE.

## References

Al-mulali, U. and Binti Che Sab, C. N.: The impact of energy consumption and $CO_2$ emission on the economic growth and financial development in the Sub Saharan African countries, Energy, 39, 180–186, doi:10.1016/j.energy.2012.01.032, 2012.

Angelbratt, J., Mellqvist, J., Simpson, D., Jonson, J. E., Blumenstock, T., Borsdorff, T., Duchatelet, P., Forster, F., Hase, F., Mahieu, E., De Mazière, M., Notholt, J., Petersen, A. K., Raffalski, U., Servais, C., Sussmann, R., Warneke, T., and Vigouroux, C.: Carbon monoxide (CO) and ethane ($C_2H_6$) trends from ground-based solar FTIR measurements at six European stations, comparison and sensitivity analysis with the EMEP model, Atmos. Chem. Phys., 11, 9253–9269, doi:10.5194/acp-11-9253-2011, 2011.

Arellano, A. F., Kasibhatla, P. S., Giglio, L., van der Werf, G. R., and Randerson, J. T.: Top-down estimates of global CO sources using MOPITT measurements, Geophys. Res. Lett., 31, L01104, doi:10.1029/2003GL018609, 2004.

Aumont, O. and Bopp, L.: Globalizing results from ocean in situ iron fertilization studies, Global Biogeochem. Cy., 20, GB2017, doi:10.1029/2005GB002591, 2006.

Bergamaschi, P., Hein, R., Heimann, M., and Crutzen, P. J.: Inverse modeling of the global CO cycle: 1. Inversion of CO mixing ratios, J. Geophys. Res., 105, 1909, doi:10.1029/1999JD900818, 2000.

Butler, T. M., Rayner, P. J., Simmonds, I., and Lawrence, M. G.: Simultaneous mass balance inverse modeling of methane and carbon monoxide, J. Geophys. Res., 110, D21310, doi:10.1029/2005JD006071, 2005.





ACPD
15, 14505–14547, 2015



Chevallier, F., Fisher, M., Peylin, P., Serrar, S., Bousquet, P., Bréon, F. M., Chédin, A., and Ciais, P.: Inferring $CO_2$ sources and sinks from satellite observations: method and application to TOVS data, J. Geophys. Res., 110, D24309, doi:10.1029/2005JD006390, 2005.

Chevallier, F., Bréon, F.-M., and Rayner, P. J.: Contribution of the Orbiting Carbon Observatory to the estimation of $CO_2$ sources and sinks: theoretical study in a variational data assimilation framework, J. Geophys. Res., 112, D09307, doi:10.1029/2006JD007375, 2007.

Chevallier, F., Fortems, A., Bousquet, P., Pison, I., Szopa, S., Devaux, M., and Hauglustaine, D. A.: African CO emissions between years 2000 and 2006 as estimated from MOPITT observations, Biogeosciences, 6, 103–111, doi:10.5194/bg-6-103-2009, 2009.

Deeter, M. N.: Operational carbon monoxide retrieval algorithm and selected results for the MOPITT instrument, J. Geophys. Res., 108, 4399, doi:10.1029/2002JD003186, 2003.

Deeter, M. N., Edwards, D. P., Gille, J. C., Emmons, L. K., Francis, G., Ho, S. P., Mao, D., Masters, D., Worden, H., Drummond, J. R., and Novelli, P. C.: The MOPITT version 4 CO product: algorithm enhancements, validation, and long-term stability, J. Geophys. Res., 115, D07306, doi:10.1029/2009JD013005, 2010.

Deeter, M. N., Martínez-Alonso, S., Edwards, D. P., Emmons, L. K., Gille, J. C., Worden, H. M., Pittman, J. V, Daube, B. C., and Wofsy, S. C.: Validation of MOPITT Version 5 thermal-infrared, near-infrared, and multispectral carbon monoxide profile retrievals for 2000–2011, J. Geophys. Res.-Atmos., 118, 6710–6725, 2013.

Deeter, M. N., Martínez-Alonso, S., Edwards, D. P., Emmons, L. K., Gille, J. C., Worden, H. M., Sweeney, C., Pittman, J. V., Daube, B. C., and Wofsy, S. C.: The MOPITT Version 6 product: algorithm enhancements and validation, Atmos. Meas. Tech., 7, 3623–3632, doi:10.5194/amt-7-3623-2014, 2014.

De Smedt, I., Stavrakou, T., Müller, J.-F., van der A, R. J., and Van Roozendael, M.: Trend detection in satellite observations of formaldehyde tropospheric columns, Geophys. Res. Lett., 37, L18808, doi:10.1029/2010GL044245, 2010.

Duncan, B. N. and Logan, J. A.: Model analysis of the factors regulating the trends and variability of carbon monoxide between 1988 and 1997, Atmos. Chem. Phys., 8, 7389–7403, doi:10.5194/acp-8-7389-2008, 2008.

Duncan, B. N., Logan, J. A., Bey, I., Megretskaia, I. A., Yantosca, R. M., Novelli, P. C., Jones, N. B., and Rinsland, C. P.: Global budget of CO, 1988–1997: source estimates and validation with a global model, J. Geophys. Res., 112, D22301, doi:10.1029/2007JD008459, 2007.





ACPD
15, 14505–14547, 2015



EPA: National Trends in CO Levels, available at: http://www.epa.gov/airtrends/carbon.html (last access: 12 February 2014), 2014.
Folberth, G. A., Hauglustaine, D. A., Lathière, J., and Brocheton, F.: Interactive chemistry in the Laboratoire de Météorologie Dynamique general circulation model: model description and impact analysis of biogenic hydrocarbons on tropospheric chemistry, Atmos. Chem. Phys., 6, 2273–2319, doi:10.5194/acp-6-2273-2006, 2006.
Folkins, I., Wennberg, P. O., Hanisco, T. F., Anderson, J. G., and Salawitch, R. J.: OH, $HO_2$, and NO in two biomass burning plumes: sources of HO−x and implications for ozone production, Geophys. Res. Lett., 24, 3185–3188, doi:10.1029/97GL03047, 1997.
Fortems-Cheiney, A., Chevallier, F., Pison, I., Bousquet, P., Carouge, C., Clerbaux, C., Coheur, P.-F., George, M., Hurtmans, D., and Szopa, S.: On the capability of IASI measurements to inform about CO surface emissions, Atmos. Chem. Phys., 9, 8735–8743, doi:10.5194/acp-9-8735-2009, 2009.
Fortems-Cheiney, A., Chevallier, F., Pison, I., Bousquet, P., Szopa, S., Deeter, M. N., and Clerbaux, C.: Ten years of CO emissions as seen from Measurements of Pollution in the Troposphere (MOPITT), J. Geophys. Res., 116, D05304, doi:10.1029/2010JD014416, 2011.
Fortems-Cheiney, A., Chevallier, F., Pison, I., Bousquet, P., Saunois, M., Szopa, S., Cressot, C., Kurosu, T. P., Chance, K., and Fried, A.: The formaldehyde budget as seen by a global-scale multi-constraint and multi-species inversion system, Atmos. Chem. Phys., 12, 6699–6721, doi:10.5194/acp-12-6699-2012, 2012.
Giglio, L., Randerson, J. T., and van der Werf, G. R.: Analysis of daily, monthly, and annual burned area using the fourth-generation global fire emissions database (GFED4), J. Geophys. Res.-Biogeo., 118, 317–328, doi:10.1002/jgrg.20042, 2013.
González Abad, G., Liu, X., Chance, K., Wang, H., Kurosu, T. P., and Suleiman, R.: Updated Smithsonian Astrophysical Observatory Ozone Monitoring Instrument (SAO OMI) formaldehyde retrieval, Atmos. Meas. Tech., 8, 19–32, doi:10.5194/amt-8-19-2015, 2015.
Granier, C., Bessagnet, B., Bond, T., D'Angiola, A., Denier van der Gon, H., Frost, G. J., Heil, A., Kaiser, J. W., Kinne, S., Klimont, Z., Kloster, S., Lamarque, J.-F., Liousse, C., Masui, T., Meleux, F., Mieville, A., Ohara, T., Raut, J.-C., Riahi, K., Schultz, M. G., Smith, S. J., Thompson, A., Aardenne, J., Werf, G. R., and Vuuren, D. P.: Evolution of anthropogenic and biomass burning emissions of air pollutants at global and regional scales during the 1980–2010 period, Climatic Change, 109, 163–190, doi:10.1007/s10584-011-0154-1, 2011.





ACPD
15, 14505–14547, 2015



Hauglustaine, D. A.: Interactive chemistry in the Laboratoire de Météorologie Dynamique general circulation model: description and background tropospheric chemistry evaluation, J. Geophys. Res., 109, D04314, doi:10.1029/2003JD003957, 2004.
Hauglustaine, D. A., Granier, C., Brasseur, G. P., and Mégie, G.: The importance of atmospheric chemistry in the calculation of radiative forcing on the climate system, J. Geophys. Res., 99, 1173, doi:10.1029/93JD02987, 1994.
Hofzumahaus, A., Rohrer, F., Lu, K., Bohn, B., Brauers, T., Chang, C.-C., Fuchs, H., Holland, F., Kita, K., Kondo, Y., Li, X., Lou, S., Shao, M., Zeng, L., Wahner, A., and Zhang, Y.: Amplified trace gas removal in the troposphere., Science, 324, 1702–1704, doi:10.1126/science.1164566, 2009.
Holloway, T., Levy, H., and Kasibhatla, P.: Global distribution of carbon monoxide, J. Geophys. Res., 105, 12123, doi:10.1029/1999JD901173, 2000.
Hooghiemstra, P. B., Krol, M. C., Bergamaschi, P., de Laat, A. T. J., Van der Werf, G. R., Novelli, P. C., Deeter, M. N., Aben, I., and Röckmann, T.: Comparing optimized CO emission estimates using MOPITT or NOAA surface network observations, J. Geophys. Res., 117, D06309, doi:10.1029/2011JD017043, 2012.
Hourdin, F., Musat, I., Bony, S., Braconnot, P., Codron, F., Dufresne, J.-L., Fairhead, L., Filiberti, M.-A., Friedlingstein, P., Grandpeix, J.-Y., Krinner, G., LeVan, P., Li, Z.-X., and Lott, F.: The LMDZ4 general circulation model: climate performance and sensitivity to parametrized physics with emphasis on tropical convection, Clim. Dynam., 27, 787–813, doi:10.1007/s00382-006-0158-0, 2006.
Jacob, D.: Introduction to Atmospheric Chemistry, Princeton University Press, Princeton, NJ, USA, 1999.
Jiang, Z., Jones, D. B. A., Worden, H. M., Deeter, M. N., Henze, D. K., Worden, J., Bowman, K. W., Brenninkmeijer, C. A. M., and Schuck, T. J.: Impact of model errors in convective transport on CO source estimates inferred from MOPITT CO retrievals, J. Geophys. Res.-Atmos., 118, 2073–2083, doi:10.1002/jgrd.50216, 2013.
Khalil, M. A. K. and Rasmussen, R. A.: Carbon monoxide in the Earth's atmosphere: indications of a global increase, Nature, 332, 242–245, 1988.
Kim, D.-H., Sexton, J. O., and Townshend, J. R.: Accelerated deforestation in the humid tropics from the 1990s to the 2000s, Geophys. Res. Lett., in press, doi:10.1002/2014GL062777, 2015.





ACPD
15, 14505–14547, 2015



Kopacz, M., Jacob, D. J., Fisher, J. A., Logan, J. A., Zhang, L., Megretskaia, I. A., Yantosca, R. M., Singh, K., Henze, D. K., Burrows, J. P., Buchwitz, M., Khlystova, I., McMillan, W. W., Gille, J. C., Edwards, D. P., Eldering, A., Thouret, V., and Nedelec, P.: Global estimates of CO sources with high resolution by adjoint inversion of multiple satellite datasets (MOPITT, AIRS, SCIAMACHY, TES), Atmos. Chem. Phys., 10, 855–876, doi:10.5194/acp-10-855-2010, 2010.

Kurokawa, J., Ohara, T., Morikawa, T., Hanayama, S., Janssens-Maenhout, G., Fukui, T., Kawashima, K., and Akimoto, H.: Emissions of air pollutants and greenhouse gases over Asian regions during 2000–2008: Regional Emission inventory in ASia (REAS) version 2, Atmos. Chem. Phys., 13, 11019–11058, doi:10.5194/acp-13-11019-2013, 2013.

Lamarque, J.-F., Bond, T. C., Eyring, V., Granier, C., Heil, A., Klimont, Z., Lee, D., Liousse, C., Mieville, A., Owen, B., Schultz, M. G., Shindell, D., Smith, S. J., Stehfest, E., Van Aardenne, J., Cooper, O. R., Kainuma, M., Mahowald, N., McConnell, J. R., Naik, V., Riahi, K., and van Vuuren, D. P.: Historical (1850–2000) gridded anthropogenic and biomass burning emissions of reactive gases and aerosols: methodology and application, Atmos. Chem. Phys., 10, 7017–7039, doi:10.5194/acp-10-7017-2010, 2010.

Lelieveld, J., Butler, T. M., Crowley, J. N., Dillon, T. J., Fischer, H., Ganzeveld, L., Harder, H., Lawrence, M. G., Martinez, M., Taraborrelli, D., and Williams, J.: Atmospheric oxidation capacity sustained by a tropical forest, Nature, 452, 737–40, doi:10.1038/nature06870, 2008.

Li, L. and Liu, Y.: Space-borne and ground observations of the characteristics of CO pollution in Beijing, 2000–2010, Atmos. Environ., 45, 2367–2372, doi:10.1016/j.atmosenv.2011.02.026, 2011.

Logan, J. A., Prather, M. J., Wofsy, S. C., and McElroy, M. B.: Tropospheric chemistry: a global perspective, J. Geophys. Res., 86, 1–45, doi:10.1029/JC086iC08p07210, 1981.

Mao, J., Ren, X., Zhang, L., Van Duin, D. M., Cohen, R. C., Park, J.-H., Goldstein, A. H., Paulot, F., Beaver, M. R., Crounse, J. D., Wennberg, P. O., DiGangi, J. P., Henry, S. B., Keutsch, F. N., Park, C., Schade, G. W., Wolfe, G. M., Thornton, J. A., and Brune, W. H.: Insights into hydroxyl measurements and atmospheric oxidation in a California forest, Atmos. Chem. Phys., 12, 8009–8020, doi:10.5194/acp-12-8009-2012, 2012.

Meyfroidt, P. and Lambin, E. F.: Global forest transition: prospects for an end to deforestation, Annu. Rev. Env. Resour., 36, 343–371, doi:10.1146/annurev-environ-090710-143732, 2011.

Naik, V., Voulgarakis, A., Fiore, A. M., Horowitz, L. W., Lamarque, J.-F., Lin, M., Prather, M. J., Young, P. J., Bergmann, D., Cameron-Smith, P. J., Cionni, I., Collins, W. J., Dalsøren, S. B.,





ACPD
15, 14505–14547, 2015



Doherty, R., Eyring, V., Faluvegi, G., Folberth, G. A., Josse, B., Lee, Y. H., MacKenzie, I. A., Nagashima, T., van Noije, T. P. C., Plummer, D. A., Righi, M., Rumbold, S. T., Skeie, R., Shindell, D. T., Stevenson, D. S., Strode, S., Sudo, K., Szopa, S., and Zeng, G.: Preindustrial to present-day changes in tropospheric hydroxyl radical and methane lifetime from the Atmospheric Chemistry and Climate Model Intercomparison Project (ACCMIP), Atmos. Chem. Phys., 13, 5277–5298, doi:10.5194/acp-13-5277-2013, 2013.

Novelli, P. C., Masarie, K. A., Lang, P. M., Hall, B. D., Myers, R. C., and Elkins, J. W.: Reanalysis of tropospheric CO trends: effects of the 1997–1998 wildfires, J. Geophys. Res.-Atmos., 108, 4464, doi:10.1029/2002JD003031, 2003.

Patra, P. K., Houweling, S., Krol, M., Bousquet, P., Belikov, D., Bergmann, D., Bian, H., Cameron-Smith, P., Chipperfield, M. P., Corbin, K., Fortems-Cheiney, A., Fraser, A., Gloor, E., Hess, P., Ito, A., Kawa, S. R., Law, R. M., Loh, Z., Maksyutov, S., Meng, L., Palmer, P. I., Prinn, R. G., Rigby, M., Saito, R., and Wilson, C.: TransCom model simulations of $CH_4$ and related species: linking transport, surface flux and chemical loss with $CH_4$ variability in the troposphere and lower stratosphere, Atmos. Chem. Phys., 11, 12813–12837, doi:10.5194/acp-11-12813-2011, 2011.

Pétron, G.: Inverse modeling of carbon monoxide surface emissions using Climate Monitoring and Diagnostics Laboratory network observations, J. Geophys. Res., 107, 4761, doi:10.1029/2001JD001305, 2002.

Pétron, G., Granier, C., Khattatov, B., Yudin, V., Lamarque, J.-F., Emmons, L., Gille, J., and Edwards, D. P.: Monthly CO surface sources inventory based on the 2000–2001 MOPITT satellite data, Geophys. Res. Lett., 31, L21107, doi:10.1029/2004GL020560, 2004.

Pison, I., Bousquet, P., Chevallier, F., Szopa, S., and Hauglustaine, D.: Multi-species inversion of $CH_4$, CO and $H_2$ emissions from surface measurements, Atmos. Chem. Phys., 9, 5281–5297, doi:10.5194/acp-9-5281-2009, 2009.

Randerson, J. T., Chen, Y., van der Werf, G. R., Rogers, B. M., and Morton, D. C.: Global burned area and biomass burning emissions from small fires, J. Geophys. Res., 117, G04012, doi:10.1029/2012JG002128, 2012.

Rayner, P. J. and O'Brien, D. M.: The utility of remotely sensed CO 2 concentration data in surface source inversions, Geophys. Res. Lett., 28, 175–178, doi:10.1029/2000GL011912, 2001.

Reuter, M., Buchwitz, M., Hilboll, A., Richter, A., Schneising, O., Hilker, M., Heymann, J., Bovensmann, H., and Burrows, J. P.: Decreasing emissions of $NO_x$ relative to $CO_2$ in East





ACPD
15, 14505–14547, 2015



Asia inferred from satellite observations, Nat. Geosci., 7, 792–795, doi:10.1038/ngeo2257, 2014.
Rohrer, F., Lu, K., Hofzumahaus, A., Bohn, B., Brauers, T., Chang, C.-C., Fuchs, H., Häseler, R., Holland, F., Hu, M., Kita, K., Kondo, Y., Li, X., Lou, S., Oebel, A., Shao, M., Zeng, L., Zhu, T., Zhang, Y., and Wahner, A.: Maximum efficiency in the hydroxyl-radical-based self-cleansing of the troposphere, Nat. Geosci., 7, 559–563, doi:10.1038/ngeo2199, 2014.
Shindell, D. T., Faluvegi, G., Stevenson, D. S., Krol, M. C., Emmons, L. K., Lamarque, J.-F., Pétron, G., Dentener, F. J., Ellingsen, K., Schultz, M. G., Wild, O., Amann, M., Atherton, C. S., Bergmann, D. J., Bey, I., Butler, T., Cofala, J., Collins, W. J., Derwent, R. G., Doherty, R. M., Drevet, J., Eskes, H. J., Fiore, A. M., Gauss, M., Hauglustaine, D. A., Horowitz, L. W., Isaksen, I. S. A., Lawrence, M. G., Montanaro, V., Müller, J.-F., Pitari, G., Prather, M. J., Pyle, J. A., Rast, S., Rodriguez, J. M., Sanderson, M. G., Savage, N. H., Strahan, S. E., Sudo, K., Szopa, S., Unger, N., van Noije, T. P. C., and Zeng, G.: Multimodel simulations of carbon monoxide: comparison with observations and projected near-future changes, J. Geophys. Res., 111, D19306, doi:10.1029/2006JD007100, 2006.
Stavrakou, T. and Müller, J.-F.: Grid-based versus big region approach for inverting CO emissions using Measurement of Pollution in the Troposphere (MOPITT) data, J. Geophys. Res., 111, D15304, doi:10.1029/2005JD006896, 2006.
Stein, O., Schultz, M. G., Bouarar, I., Clark, H., Huijnen, V., Gaudel, A., George, M., and Clerbaux, C.: On the wintertime low bias of Northern Hemisphere carbon monoxide found in global model simulations, Atmos. Chem. Phys., 14, 9295–9316, doi:10.5194/acp-14-9295-2014, 2014.
Stocker, T. F., Qin, D., Plattner, G.-K., Tignor, M., Allen, S. K., Boschung, J., Nauels, A., Xia, Y., Bex, V., and Midgley, P. M.: IPCC, 2013: Summary for Policymakers, in: Climate Change 2013: The Physical Science Basis, Working Group I Contribution to the Fifth Assessment Report of the Intergovernmental Panel on Climate Change-Abstract for Decision-Makers, Cambridge University Press, Cambridge, United Kingdom and New York, NY, USA, 2013.
Thompson, A. M.: The oxidizing capacity of the earth's atmosphere: probable past and future changes, Science, 256, 1157–1165, doi:10.1126/science.256.5060.1157, 1992.
Tohjima, Y., Kubo, M., Minejima, C., Mukai, H., Tanimoto, H., Ganshin, A., Maksyutov, S., Katsumata, K., Machida, T., and Kita, K.: Temporal changes in the emissions of $CH_4$ and CO from China estimated from $CH_4/CO_2$ and $CO/CO_2$ correlations observed at Hateruma Island, Atmos. Chem. Phys., 14, 1663–1677, doi:10.5194/acp-14-1663-2014, 2014.





ACPD
15, 14505–14547, 2015



van der Werf, G. R., Randerson, J. T., Giglio, L., Collatz, G. J., Kasibhatla, P. S., and Arellano Jr., A. F.: Interannual variability in global biomass burning emissions from 1997 to 2004, Atmos. Chem. Phys., 6, 3423–3441, doi:10.5194/acp-6-3423-2006, 2006.

van der Werf, G. R., Randerson, J. T., Giglio, L., Collatz, G. J., Mu, M., Kasibhatla, P. S., Morton, D. C., DeFries, R. S., Jin, Y., and van Leeuwen, T. T.: Global fire emissions and the contribution of deforestation, savanna, forest, agricultural, and peat fires (1997–2009), Atmos. Chem. Phys., 10, 11707–11735, doi:10.5194/acp-10-11707-2010, 2010.

Van Leeuwen, T. T., Peters, W., Krol, M. C., and van der Werf, G. R.: Dynamic biomass burning emission factors and their impact on atmospheric CO mixing ratios, J. Geophys. Res.-Atmos., 118, 6797–6815, doi:10.1002/jgrd.50478, 2013.

Wang, R., Tao, S., Shen, H., Huang, Y., Chen, H., Balkanski, Y., Boucher, O., Ciais, P., Shen, G., Li, W., Zhang, Y., Chen, Y., Lin, N., Su, S., Li, B., Liu, J., and Liu, W.: Trend in global black carbon emissions from 1960 to 2007, Environ. Sci. Technol., 48, 6780–6787, doi:10.1021/es5021422, 2014.

Worden, H. M., Deeter, M. N., Frankenberg, C., George, M., Nichitiu, F., Worden, J., Aben, I., Bowman, K. W., Clerbaux, C., Coheur, P. F., de Laat, A. T. J., Detweiler, R., Drummond, J. R., Edwards, D. P., Gille, J. C., Hurtmans, D., Luo, M., Martínez-Alonso, S., Massie, S., Pfister, G., and Warner, J. X.: Decadal record of satellite carbon monoxide observations, Atmos. Chem. Phys., 13, 837–850, doi:10.5194/acp-13-837-2013, 2013.

Yevich, R. and Logan, J. A.: An assessment of biofuel use and burning of agricultural waste in the developing world, Global Biogeochem. Cy., 17, 1059, doi:10.1029/2002GB001952, 2003.

Yoon, J. and Pozzer, A.: Model-simulated trend of surface carbon monoxide for the 2001–2010 decade, Atmos. Chem. Phys., 14, 10465–10482, doi:10.5194/acp-14-10465-2014, 2014.

Yoon, J., Pozzer, A., Hoor, P., Chang, D. Y., Beirle, S., Wagner, T., Schloegl, S., Lelieveld, J., and Worden, H. M.: Technical Note: Temporal change in averaging kernels as a source of uncertainty in trend estimates of carbon monoxide retrieved from MOPITT, Atmos. Chem. Phys., 13, 11307–11316, doi:10.5194/acp-13-11307-2013, 2013.

Zellweger, C., Hüglin, C., Klausen, J., Steinbacher, M., Vollmer, M., and Buchmann, B.: Intercomparison of four different carbon monoxide measurement techniques and evaluation of the long-term carbon monoxide time series of Jungfraujoch, Atmos. Chem. Phys., 9, 3491–3503, doi:10.5194/acp-9-3491-2009, 2009.





ACPD
15, 14505–14547, 2015



**Table 1.** Prior datasets for the sources and sinks of CO. Mean annual sums are calculated for the period from 2002 to 2011. The global annual prior error bugets are reported and TransCom-OH field is used.

| | Sectors | Mean Annual Sum ($Tg\,yr^{-1}$) | Dataset/ Model | References |
|---|---|---|---|---|
| CO | Sources: | | | |
| | Biomass burning | 327 | GFEDv3.1 | Van der Werf et al. (2010) |
| | Anthropogenic Emissions | 588 | MACCity | Lamarque et al. (2010) |
| | Ocean | 54 | PISCES | Belattaf et al. (2012) |
| | Sum of surface emissions | $969 \pm 180$[1] | | |
| | Oxidation from NMVOC | $335 \pm 43$[2] | LMDz-INCA | Folberth et al. (2006) |
| | Oxidation from $CH_4$ | $885 \pm 92$[3] | | |
| | Sum of chemical sources | 1220 | | |
| | Sinks: | | | |
| | Oxidation by OH | 2197 | TransCom-OH | Patra et al. (2011) |

[1] The uncertainty represents the SD of the global annual error budgets in the prior CO emissions in the inversion configuration.
[2] The SD is calculated into the equivalent CO amount from global annual error budgets of the pre-calculated $CH_2O$ production fields.
[3] The SD is calculated into the equivalent CO amount from global annual error budgets of the prior $CH_4$ emissions assuming they are all oxidized into CO in a single step. The prior $CH_4$ emission ($506\,TgCO\,yr^{-1}$) datasets are detailed in Cressot et al. (2014).





ACPD
15, 14505–14547, 2015



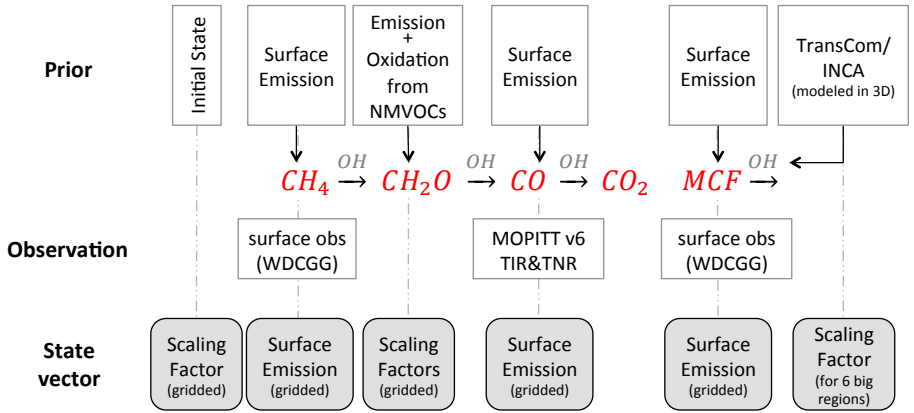


**Figure 1.** Schematics of the input information provided to the inversion and of the inversion state vector.





ACPD
15, 14505–14547, 2015



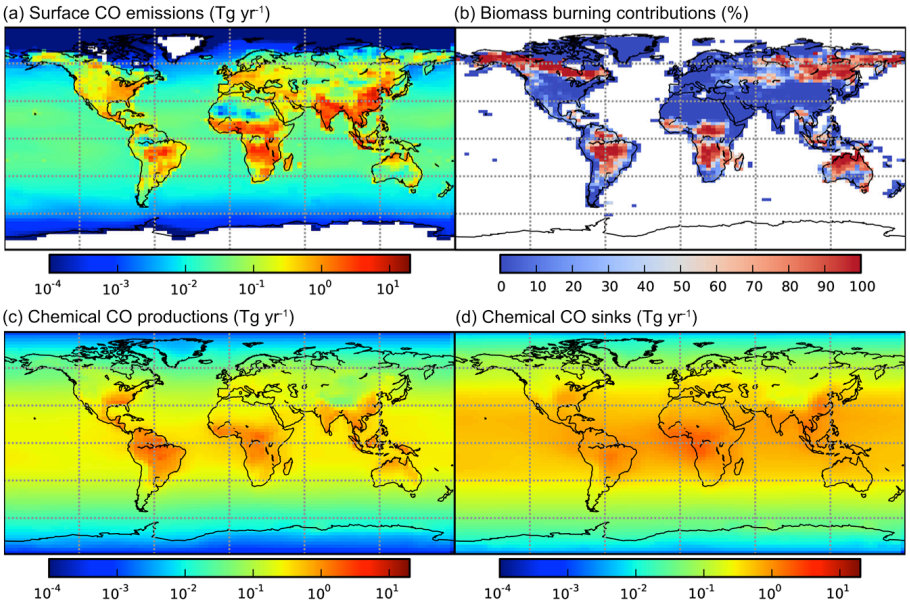


**Figure 2.** Distribution of prior budget terms for CO. Mean values from 2002 to 2011 are shown. **(a)** Surface CO emissions, **(b)** relative percentages of CO emissions from biomass burning over land, **(c)** atmospheric CO productions from $CH_4$ and NMVOC, **(d)** atmopsheric CO chemical sinks. The chemical productions and sinks are calculated with TransCom-OH.





ACPD
15, 14505–14547, 2015



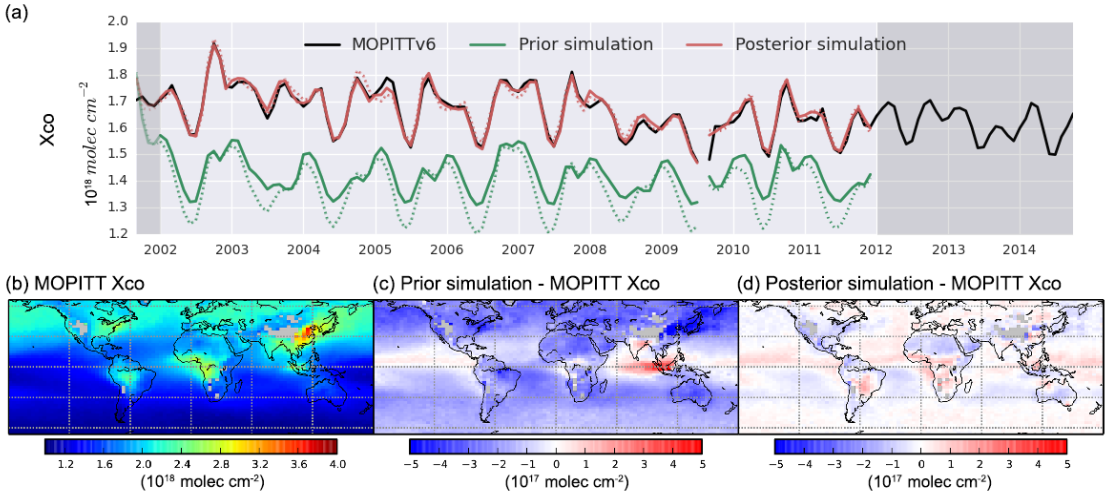


**Figure 3.** Time series and spatial distributions of CO total column ($X_{CO}$). **(a)** Time series of global monthly mean $X_{CO}$. The black line represents satellite observation of MOPITTv6 $X_{CO}$, the green (red) lines represent the prior (posterior) simulations. Solid lines represent the control version with TransCom-OH, and doted lines represent the test with INCA-OH. The grey-shaded area is for display only and is not included in the trend analysis in this paper. **(b)** Distribution of multi-year mean annual $X_{CO}$ of MOPITTv6 retrieval. **(c)** Mean annual difference between the prior simulation and MOPITT. **(d)** Mean annual difference between the posterior simulation and MOPITT. Simulations shown in c and d used TransCom-OH. The results with INCA-OH show similar spatial distributions and are not shown here.





ACPD
15, 14505–14547, 2015



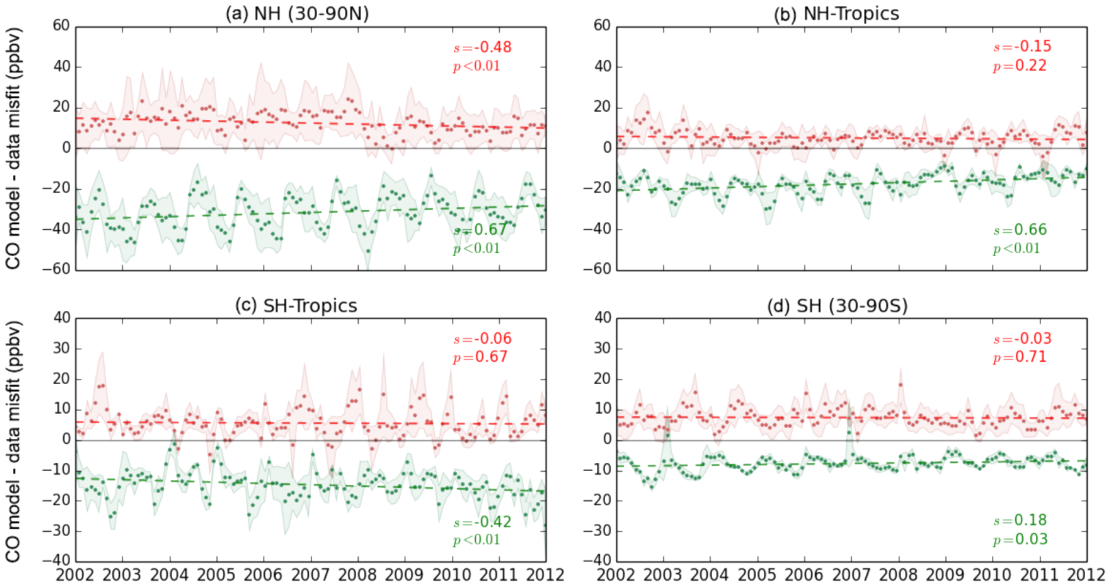


**Figure 4.** Time series of monthly mean CO misfits between the prior (green) and the posterior (red) simulations against surface measurements in each latitudinal band. The shaded areas represent the spatial SD among the sites in each zone. The dashed lines represent linear regressions, and "*s*" and "*p*" denote the slope and *p* value of the regression.





ACPD
15, 14505–14547, 2015



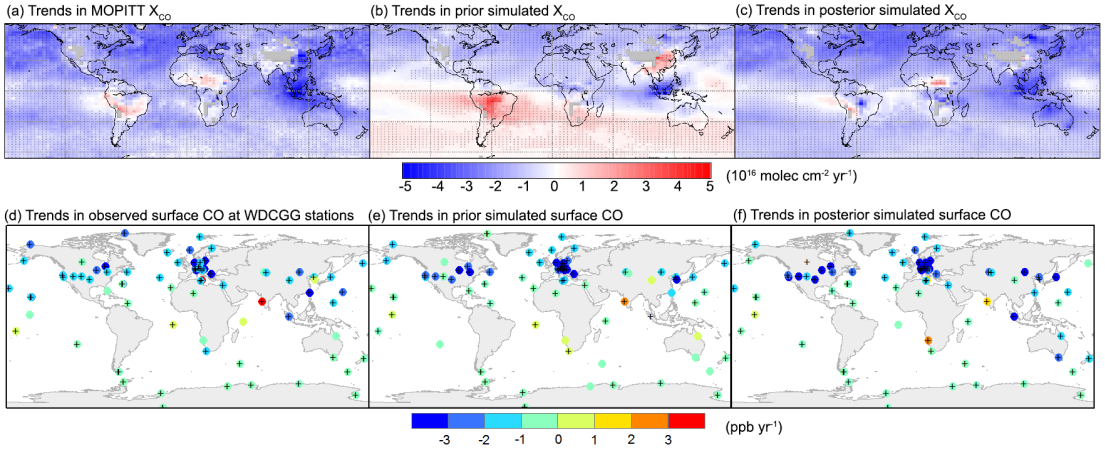


**Figure 5.** Distribution of CO concentration trends from 2002 to 2011. The upper row successively shows $X_{CO}$ trends in **(a)** MOPITTv6 retrievals, **(b)** the prior and **(c)** the posterior simulation. The lower row shows the CO concentration trends at **(d)** the surface stations from WDCGG and corresponding **(e)** prior and **(f)** posterior trends at those stations. Black crosses indicate significance at 95 % confidence level. Different colour bars are used for $X_{CO}$ and surface CO concentrations, and the two values are not directly comparable.





ACPD
15, 14505–14547, 2015



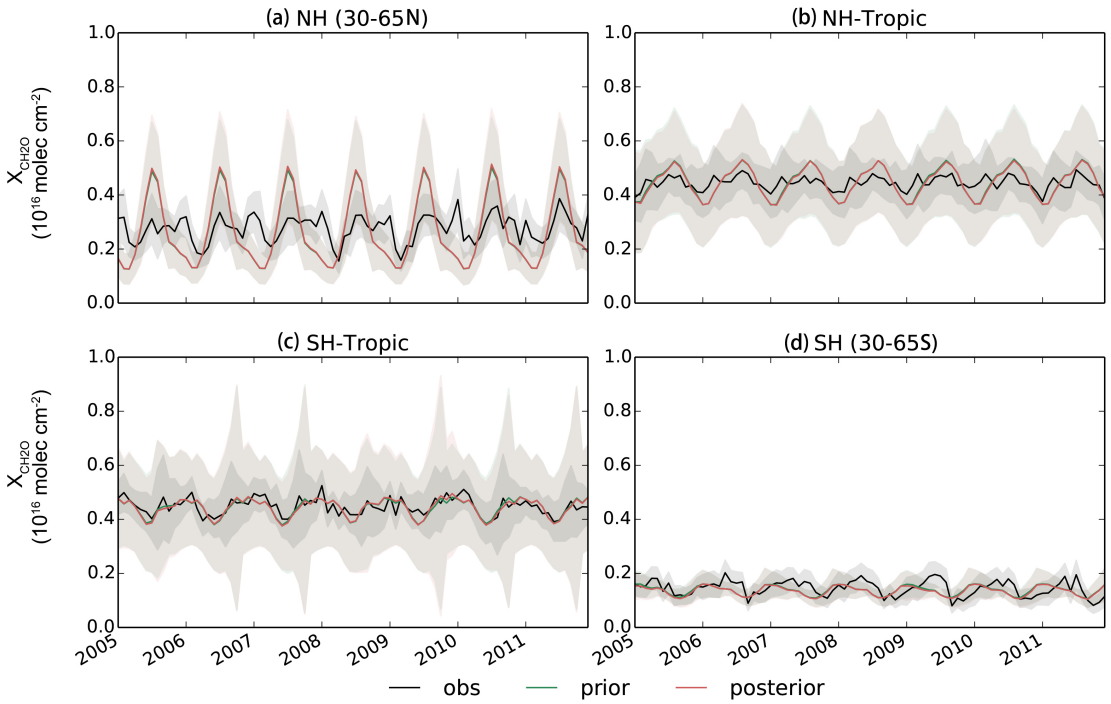


**Figure 6.** Time series of $CH_2O$ total column averaged by latitudinal bands. The black lines indicate the $CH_2O$ total column from SAO OMI retrievals, green lines indicate prior simulations, and red lines indicate posterior simulations. Shading areas show the SD within a latitudinal band. The forward and posterior simulations nearly overlay each other.





ACPD
15, 14505–14547, 2015



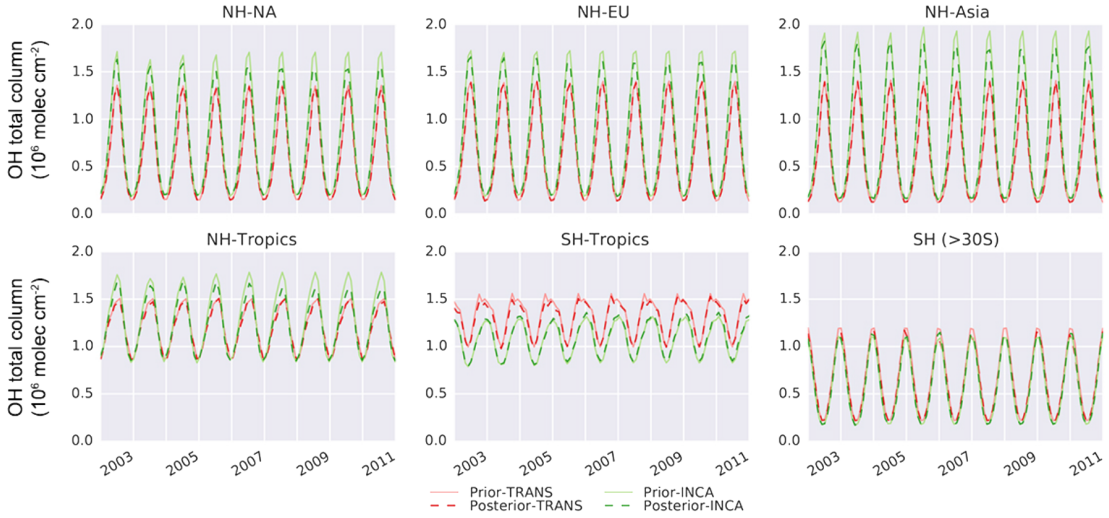


**Figure 7.** Regional volume-weighted monthly mean OH concentrations in the prior and posterior. The results are shown for the 6 big regions in which OH is optimized.





ACPD
15, 14505–14547, 2015



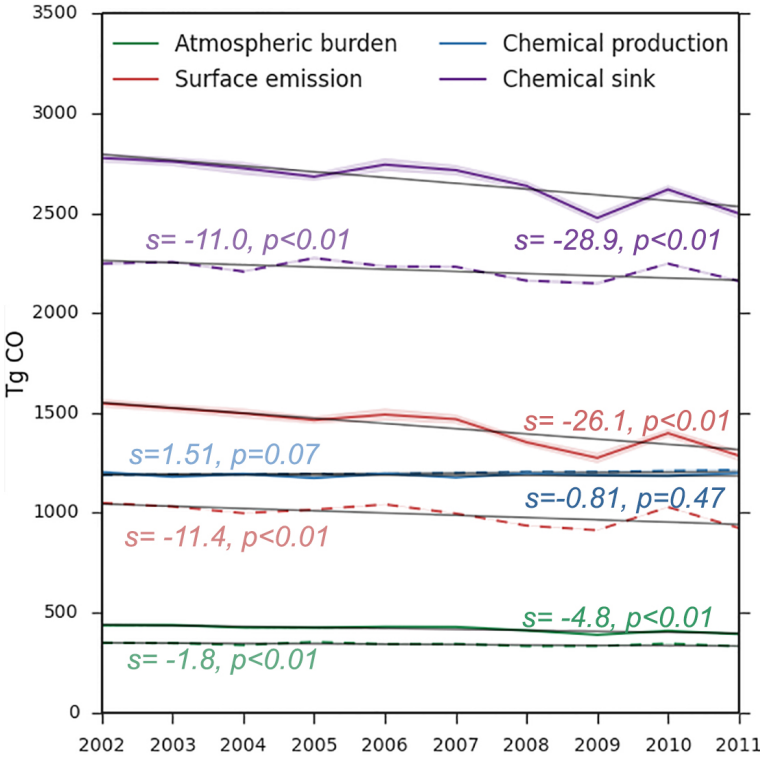


**Figure 8.** Time series of global mean annual CO budget changes from 2002 to 2011. Dashed lines indicate prior values and solid lines indicate posterior values in corresponding items. Beside each line, s denotes the linear slope and p denotes the *p* value for the regression analysis.





ACPD
15, 14505–14547, 2015



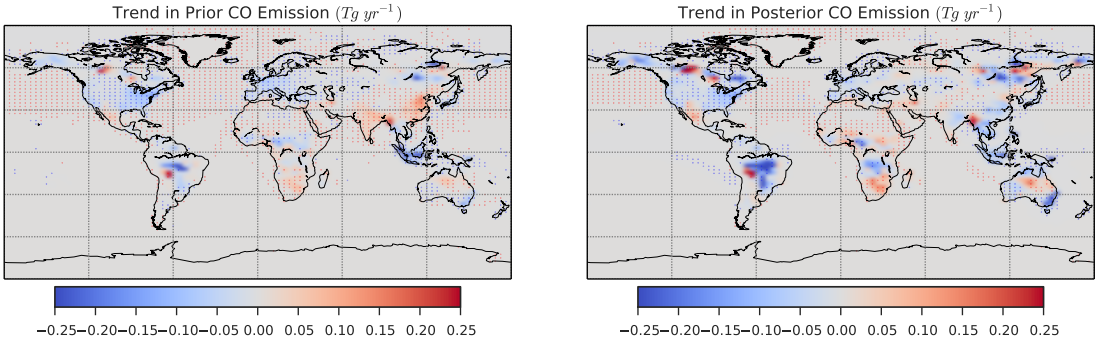


**Figure 9.** Trends distributions of CO surface emissions in the prior and in the posterior from 2002 to 2011.





ACPD
15, 14505–14547, 2015



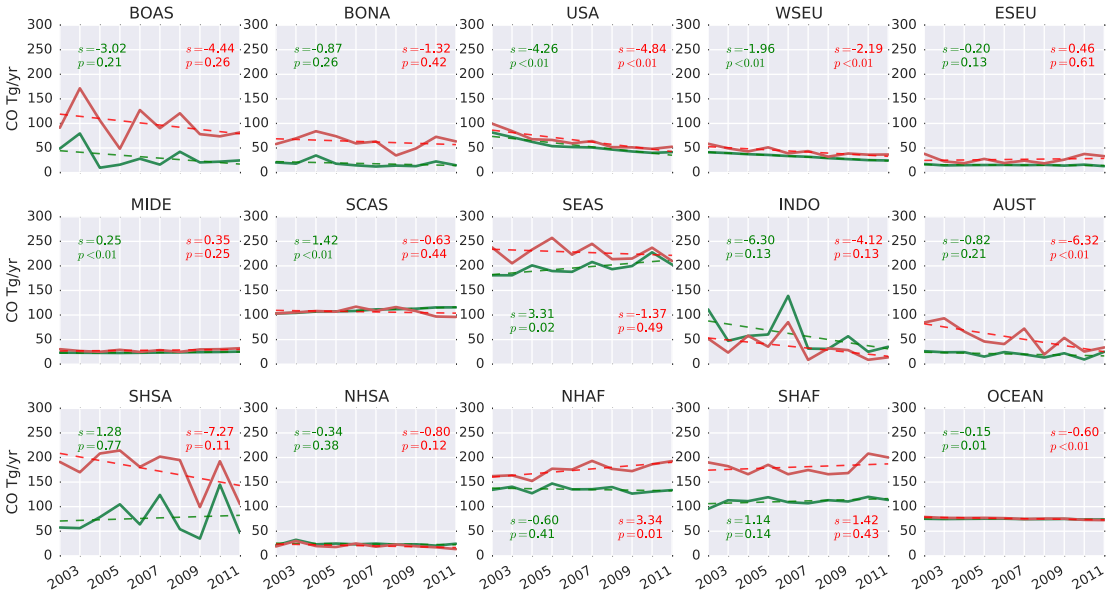


**Figure 10.** Annual prior (green) and posterior (red) CO emissions in each sub-region from 2002 to 2011. The dash lines represent linear regressions, beside which s denotes the linear slope and p denotes the *p* value for the regression. The notation for the sub-regions are listed as follows and the extent of each region is shown in Fig. S1. BOAS – Boreal Asia, BONA – Boreal North America, USA – USA, WSEU – West Europe, ESEU – East Europe, MIDE – Middle East, SCAS – South Central Asia, SEAS – South East Asia, INDO- Indonesia, AUST – Australia, NHSA- North Hemisphere South America, SHSA – South Hemisphere South America, NHAF – North Hemisphere Africa, SHAF – South Hemisphere Africa, OCEAN – all ocean emissions both biogenic and anthropogenic emissions.





ACPD
15, 14505–14547, 2015



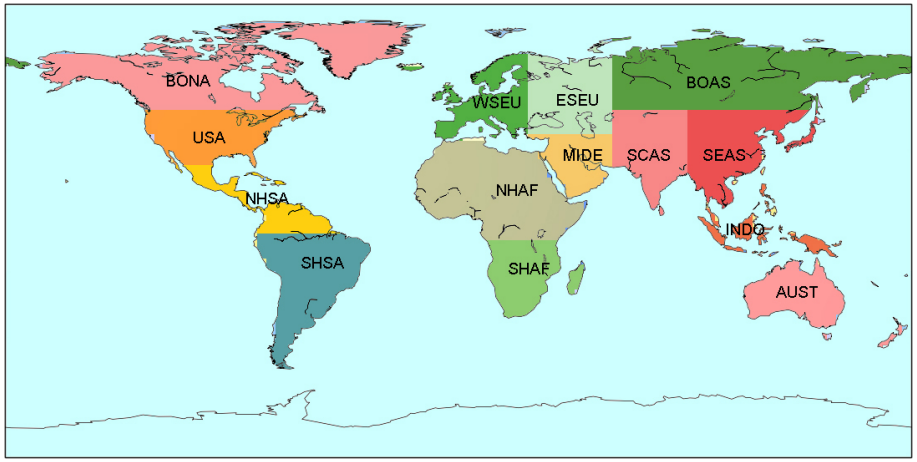


**Figure A1.** Sub-region extent.





ACPD
15, 14505–14547, 2015